crystals

MDPI

Article

Investigation of Copper as Collector Metal in Sodium-Oxide Fluxed Aluminothermic Reduction of Manganese Ore

Theresa Coetsee [1,*] and Frederik De Bruin [2]

[1] Department of Materials Science and Metallurgical Engineering, University of Pretoria, Pretoria 0002, South Africa
[2] Independent Metallurgical Consultant, Pretoria 0002, South Africa; fjdb.1953@gmail.com
* Correspondence: theresa.coetsee@up.ac.za

Abstract

Aluminothermic reduction is gaining renewed interest as an alternative processing route for the circular economy. A unique Na_2O-fluxed MnO_2 ore formulation with a small quantity of carbon reductant was applied to ensure rapid pre-reduction to MnO. This approach negates the pre-roasting step. The Na_2O flux enables the formation of the water-soluble compound, $NaAlO_2$, which enables recycling of Al_2O_3 for aluminium production. The addition of copper as a collector metal improved the overall alloy yield from 43% to 57%, which includes a 6% increase in Mn recovery to the alloy. The product alloy is a medium-carbon Fe–Mn–Si–Al–Cu complex ferroalloy that can be used as a steelmaking ferroalloy additive. The ferroalloy consists of 54% Mn, 19% Fe, 2.1% Si, 2.6% Al, 21% Cu, and 1.2% C. This carbon content is modulated by low-carbon solubility copper, despite the use of a graphite crucible. The formulated slag exhibits high Al_2O_3 solubility, enabling effective alloy–slag separation from the high Al_2O_3 content slag of 52% Al_2O_3. Gas–slag–metal equilibrium calculations for 1650 °C–1950 °C overlap with the experimentally produced alloy chemistry in %C and %Si, but not the %Al, as the uptake of aluminium exceeds the equilibrium calculation at 0.03–0.17%.

Keywords: aluminothermic; alloy yield; manganese ore; circular economy; collector metal; sustainable processing; copper; complex ferroalloy; flux

1. Introduction

Aluminothermic reduction in MnO_2-type manganese ore is applied to produce low-carbon ferromanganese alloy. The MnO_2 ore is pre-roasted to convert MnO_2 to lower oxidation state oxides of Mn_2O_3 and Mn_3O_4 to avoid violent heat release from aluminothermic reduction in MnO_2 [1]. The negative consequences of violent heat release are substantial metal losses due to vaporisation and the safety hazard of the likely expulsion of molten materials. The ore feed requirement includes a minimum manganese content of 46% Mn, a minimum manganese-to-iron ratio of nine, and a phosphorus content limited to 0.12% P. Furthermore, this pure ore is fluxed with CaF_2 to enable good alloy–slag separation. The aluminothermic method was applied at the scale of 3–10 kg feed mixture and produced alloy of 70–84% Mn, 13–16% Fe, 1–10% Si, <0.03% Al, and <0.24% P, with a metal yield of 58–64% [1]. In addition to the use of MnO_2 ore, the aluminothermic reduction in MnO-containing slags attracts increased research attention [2,3]. This is because the Al_2O_3 product from the aluminothermic reduction can be recycled for use in the Hall–Héroult process after undergoing hydrometallurgical treatment [4,5]. Furthermore, this processing

Academic Editor: Umberto Prisco

Received: 19 December 2025
Revised: 7 January 2026
Accepted: 8 January 2026
Published: 11 January 2026

approach limits CO_2 emissions if the electricity input to the Hall–Héroult process is sourced from non-fossil fuel energy sources. This processing alternative is also attracting research interest in the recycling of waste streams, such as end-of-life lithium-ion batteries and waste iron oxides, including mill-scale [6–8].

By changing the slag design to utilise sodium oxide flux, instead of CaF_2 or CaO–Al_2O_3-based slags, the Al_2O_3 product from the aluminothermic reduction process can be recycled with ease due to the formation of $NaAlO_2$ as a water-soluble compound [5]. In recent work, the application of sodium oxide fluxed aluminothermic reduction in MnO_2 ore, assisted by small quantities of coal addition and collector metals of Si and Cr, was demonstrated [9,10]. The results are summarised in Table 1. It is observed that the addition of Si and Cr collector metals improved the alloy yield and reduced the alloy carbon content to levels below the alloy carbon saturation limit. A small quantity of coal was added to reduce MnO_2 to MnO before the aluminothermic reaction starts to avoid the violent reaction of MnO_2 with aluminium. In this way, the additional step of pre-roasting the MnO_2 ore, as described by Bhoi et al. [1], was removed.

Table 1. Results from sodium oxide-fluxed aluminothermic reduction in MnO_2 ore [9,10].

Feed Mixture	%Mn	%Fe	%Al	%C	%Si	%Cr	%Alloy Yield	Saturation %C at 1550 °C
MnO_2–C	66	28	0.4	3.5	1.4	0	43	6.5
MnO_2–C–Si	66	22	1.4	2.2	8.7	0	56	4.2
MnO_2–C–Cr	57	18	1.5	2.2	3.4	18	68	6.9

The application of aluminium–silicon–manganese (AMS), ferromanganese–aluminium (FMA), and ferrosilicon–manganese–aluminium (FAMS) complex ferroalloys in conventional steelmaking plants is more efficient than adding individual deoxidiser alloys [11,12]. These alloys are produced in electric furnaces operated at high temperatures using coke as a reductant to reduce Al_2O_3 to Al [11]. However, this processing option does not account for circular processing and CO_2 emissions reduction. Table 2 summarises the composition bands of complex ferroalloys in comparison to ferromanganese alloys [11–13]. Thermic reduction with aluminium or silicon as reductant is a well-established method of producing low-carbon ferromanganese from a molten slag [14]. Medium-carbon ferromanganese (MCFeMn) can be produced by thermic reduction or via oxygen refining of high-carbon ferromanganese (HCFeMn). Silicothermic reduction of manganese from slags is performed in an electric furnace. The extra arc heat is required because insufficient exothermic heat is generated in the silicothermic reduction reactions [14]. Low-carbon ferromanganese (LCFeMn) is only produced with silicothermic reduction because of excessive manganese losses in oxygen refining. Complex reducing agents in the form of furnace dusts, AlSiMn and FeSiAl, can be applied to produce Fe–Cr–Mn–Si alloys from low-grade manganese and chromium ore [15]. Electric arc furnace energy is applied, since insufficient chemical energy is available to sustain a SHS (self-propagating high-temperature synthesis) process. This processing approach is similar to the recycling of manganese slag with aluminium dross [2,3].

Although the aluminothermic process was pioneered in 1859 by Beketov, research continues on the optimal application arrangements of the aluminium reduction reactions [16]. It has been demonstrated that the chemical composition and particle size of the feed material significantly influence the aluminothermic reaction rate and extent, thereby determining the maximum attained temperature and the final product proportions and chemistries [1,7–10,17,18]. Therefore, empirical testing of the aluminothermic reaction assembly is required to reach the optimum reaction conditions. For example, in the reaction of MnO_2–Al at laboratory-scale, it was found that the reaction mixture did not react under

Argon gas, and the reaction only proceeded in the presence of air [17]. Another example is the application of aluminothermic reduction in various welding processes to add extra heat energy to the welding process via reaction with oxides, such as CuO, MnO_2, and Fe_2O_3, in self-shielded flux-cored arc welding (FCAW–S), which requires careful control of the input formulations [19–21].

Table 2. Ferromanganese alloy compositions (mass%); n.s. = not specified [11–13].

	%Mn	%Si	%C	%P	%S	%Al
HCFeMn (A)	78–82	<1.2	<7.5	<0.35	<0.02	n.s.
MCFeMn (A)	80–85	<1.5	<1.5	<0.30	<0.02	n.s.
LCFeMn (B)	80–85	5.0–7.0	<0.75	<0.30	<0.02	n.s.
AMS	60–70	5–15	0.4–2.0	<0.05	n.s.	8–20
FMA	40–80	<2.5	<1.5	<0.3	<0.03	12–16
FAMS	22–24	10–15	1–2	<0.06	n.s.	10–14

New-generation steel grades utilise copper as an alloying element to enhance their material properties. For example, 2–4% Cu-containing chrome–manganese stainless steel grades are used to improve their corrosion resistance, and corrosion-resistant rebar contains 0.4–0.45% Cu [22]. Copper is applied as a cost-effective wear-resistant alloying element (up to 1.1% Cu) to increase the wear resistance of low-carbon steel and to higher levels of 2–7% Cu in Fe–Cr–Cu–Ti FCAW–S-deposited hardfacing alloys [23,24]. Copper is added to biomaterials due to its antimicrobial properties, for example, in Fe–Mn–Cu alloy implants [25]. Therefore, a copper-containing complex ferroalloy based on the FMA ferroalloy may be applied as a steelmaking additive.

The objective of this work is to produce a complex ferroalloy of Fe–Mn–Si–Al–Cu with medium-carbon content from a Na_2O-fluxed feed mixture formulation for the circular aluminothermic reduction of manganese ore. Copper was added as a collector metal to improve the alloy yield. A successful slag formulation must achieve high Al_2O_3 solubility to facilitate adequate alloy–slag separation and produce slag containing the water-soluble compound $NaAlO_2$, which enables the hydrometallurgical recovery of aluminium.

2. Materials and Methods

The materials and methods presented below are identical to those used in the authors' recent work [9,10].

2.1. Methodology

The experimental methodology, as shown in Figure 1, consists of various interdependent calculation steps to specify the feed mixture for application in the experiments. A simple mass balance was applied to calculate the carbon and aluminium reductant additions and the proportions of fluxes, namely $Na_2O.SiO_2$, and CaO, aimed at a basicity ratio (%CaO/%SiO_2) equal to one. The slag was designed to crystallise the desired $NaAlO_2$ compound on cooling. The slag composition is required firstly to have high solubility of Al_2O_3 and good fluidity to ensure good alloy–slag separation at an estimated lower temperature of 1450 °C, 100 °C higher than the target slag's liquidus temperature. The alloy should have a solidus and liquidus temperature below or close to the slag solidus temperature to ensure the maximum possibility of slag–alloy separation. The attained alloy %C is not certain, and alloy composition calculations were made with the assumption of 0–3% C.

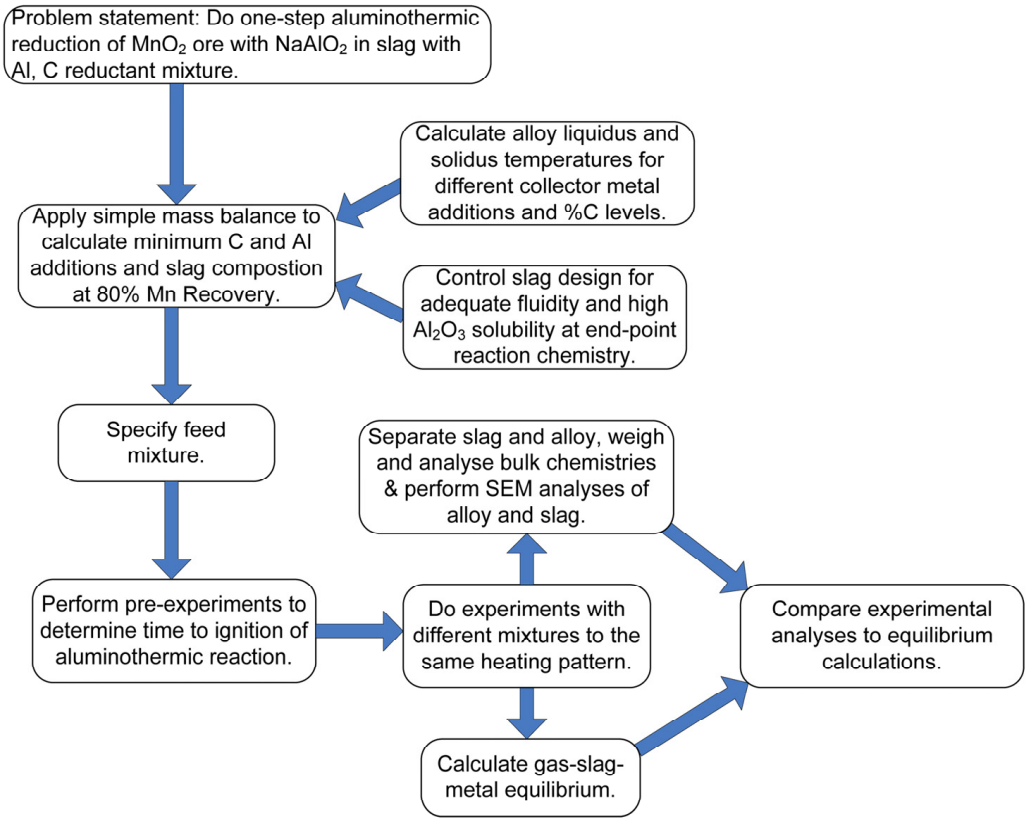

Figure 1. Experimental methodology.

2.2. Materials

The experimental setup utilised manganese ore, coal, aluminium, and copper metal powders, along with lime and sodium silicate as fluxing agents. High-purity aluminium (99.7%, particle size below 1 mm) was sourced from Sigma–Aldrich in Johannesburg, South Africa. Copper powder (99.8%, particle size below 200 µm) was obtained from Alfa Aesar, also in Johannesburg. Sodium silicate and calcium oxide were supplied by Sigma–Aldrich and Associated Chemical Enterprises, respectively, both located in Johannesburg, South-Africa. The manganese ore of particle sizes below 6.3 mm, primarily pyrolusite (MnO_2), and the medium-volatile coal of particle sizes below 2 mm were both acquired from local deposits in South Africa. The coal's composition includes 22.5% volatile matter, 12% ash, 62.2% fixed carbon, and 3.3% moisture. Analytical data for both the ore and coal ash are presented in Table 3. For each experiment, the mixture was prepared using 100 g of ore placed in a graphite crucible with a matching graphite lid. The crucible measured 50 mm in diameter, 70 mm in height, and had a wall thickness of 7 mm, with the lid recessed to fit securely. Graphite crucibles were supplied by SGL Carbon (Pty) Ltd., Johannesburg, South Africa. The graphite material is R4340 graphite, suitable for alloy continuous casting dies, and has 15 µm grain size, 200 ppm ash content, and apparent density of 1.72 g/cm^3. Table 4 summarises the different reaction mixtures used.

Table 3. Bulk chemical composition of manganese ore and coal ash (mass%).

	%FeO	%MnO	%Cr_2O_3	%V_2O_5	%TiO_2	%CaO	%K_2O	%P_2O_5	%SiO_2	%Al_2O_3	%MgO	%Na_2O	%BaO
Ore	10.70	61.59	0.03	0.04	0.05	0.23	0.21	0.01	5.43	2.61	0.11	0.00	1.85
Ash	1.51	0.02	0.05	0.05	2.16	2.46	0.51	1.19	51.44	39.35	0.68	0.30	0.27

Table 4. Reaction mixtures (grams).

	Ore	Coal	$Na_2O.SiO_2$	CaO	Al	Cu
Base case (BC)	100	27	20	15	0	0
A	100	10	20	15	30	0
B	100	10	20	15	30	10

2.3. Methods

2.3.1. Experimental Procedure

All components were weighed and thoroughly blended before being transferred into the graphite crucible, which was then sealed with the crucible lid. The muffle furnace was preheated and maintained at 1350 °C for 12 h using a PID controller for temperature regulation. The aluminothermic reaction was initiated by placing the crucible in the furnace. Based on previous trials, the crucible was removed two minutes after ignition, which was indicated by a visible flame at the furnace's side panel joints. The heating of the mixture was primarily due to the exothermic aluminothermic reaction rather than the furnace itself. Ignition occurred six minutes after insertion, and the total reaction time was eight minutes. After removal, the lid was taken off, and the molten alloy and slag were poured into a cast-iron mould. Once cooled to room temperature, the contents were returned to the crucible for manual separation of the metal and slag.

2.3.2. Material Analysis

Sections of the separated alloy and slag were analysed for chemical composition using scanning electron microscopy (SEM) equipped with energy-dispersive X-ray spectroscopy (EDX), Zeiss 540 Ultra FEG SEM (Zeiss, Oberkochen, Germany). The cross-sections were gold-coated. Inductively coupled plasma optical emission spectroscopy (ICP–OES) was performed using a PerkinElmer Optima 5300 instrument (Perkin Elmer, Springfield, IL, USA) to analyse the ore, alloy, and slag samples in bulk form. Carbon and sulphur content in the alloy were measured by combustion analysis using a LECO CS 744 instrument (LECO, St Joseph, MO, USA). Coal was analysed according to the South African National Standard (SANS 17246:2011) [26] and coal ash composition was determined by X-ray fluorescence (XRF) using an ARL Advant'X Series Sequential Intellipower^{TM} XRF instrument (Thermo Fisher Scientific, Waltham, MA, USA).

2.3.3. Thermochemical Modelling

Equilibrium phase compositions for the alloys were calculated using Thermo–Calc 2023b software with the SGTE Alloy 4.9 database [27]. Slag equilibrium and gas–slag–metal interactions for the samples were modelled using FactSage 7.3, employing the FToxid and SGTE databases. The Equlib module in FactSage was used in these calculations [28]. The Equilib module free energy minimisation routine calculated the equilibrium gas, slag, and metal compositions for the user-specified inputs of temperature and the chemistries and mass proportions of ore, fluxes ($Na_2O.SiO_2$, CaO), Cu collector metal, and coal carbon. Therefore, the calculations are not constrained or modified in any way from the inherent Equilib free energy minimisation calculation.

3. Results

For comparison purposes, Figure 2a of the base case (BC) Sample with no Al or collector metals added, as well as Figure 2b with only Al added, are shown, as in our prior work [9,10]. Figure 2c from Sample B shows a large alloy volume and some smaller alloy particles formed from adding Cu as a collector metal, similar to Figure 2b. The copper-based alloy appears larger in size than that shown in Figure 2b for Sample A, with

no collector metal added. In both cases of Samples A and B, good alloy–slag separation was achieved.

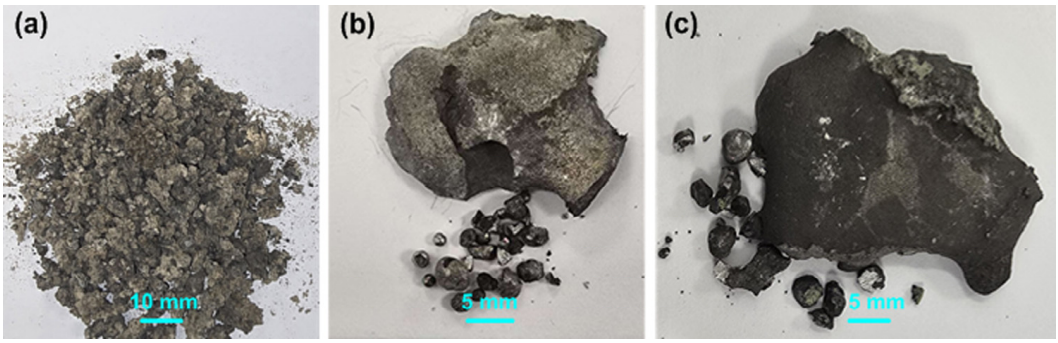

Figure 2. (**a**) Photographs of magnetic fraction from Sample BC; (**b**) easily separated alloy from Sample A; (**c**) easily separated alloy from Sample B.

In contrast, the magnetic fraction of the base case (BC) sample, as shown in Figure 2a, confirms that insignificant slag and alloy formed at the muffle furnace temperature (1350 °C). The reason for this low level of reduction is the low heat input in the absence of exothermic heat, resulting in low reduction rates. Due to the endothermic Boudouard reaction versus the exothermic aluminium reaction, a much longer dwell time in the furnace would be needed to achieve noticeable alloy formation via carbothermic reduction. It is well known from carbothermic reduction studies on various ferruginous manganese ores that the reduction of manganese oxides to manganese metal is possible in the presence of carbon at low reaction temperatures, as low as 1000 °C. The thermodynamic favourability of the reduction reaction at such low temperatures is due to high MnO activity and low Mn activity in the presence of initially formed Fe [29–31].

The fractured surfaces of the large alloy volumes from Samples A and B were analysed by SEM–EDX. A typical analysis area consisted of 0.5 mm × 0.5 mm. EDX element maps and SEM images of example areas comprising the field of view (FOV) from each alloy are displayed in Figures 3–5. The analyses of the areas are summarised in Tables 5 and 6. The maximum variance (σ) of the SEM–EDX analyses for each element is also indicated. The bulk chemistry of each alloy is displayed in Tables 5 and 6, specifically, because the SEM–EDX does not accurately analyse for carbon, whilst the LECO combustion analysis of the bulk alloy provides quantitative %C. The Sample A alloy in Figure 3 appears to be a dense homogeneous single-phase alloy of Mn, Fe, and Si. The Sample A alloy bulk analysis and SEM–EDX analyses are similar.

Table 5. EDS analyses of Sample A alloy (mass%); n.a. = not available; n.d. = not detected.

Area	%Al	%Si	%Mn	%Fe	%Ca	%V	%S	%C
1	0.6	2.4	69.4	26.9	0.1	0.6	0.0	n.a.
2	0.0	2.2	68.8	28.3	0.2	0.6	0.0	n.a.
3	1.6	2.3	68.2	27.0	0.2	0.6	0.0	n.a.
4	0.8	2.1	68.1	28.3	0.1	0.6	0.0	n.a.
5	1.4	1.8	67.5	28.6	0.2	0.6	0.0	n.a.
Average	0.9	2.2	68.4	27.8	0.2	0.6	0.0	n.a.
Maximum σ	0.01	0.01	0.06	0.03	0.00	0.01	n.d.	
Bulk Alloy	0.4	1.4	66.1	28.0	0.05	0.40	0.03	3.5

Table 6. EDS analyses of Sample B alloy (mass%); n.a. = not available.

Area	%Al	%Si	%Mn	%Fe	%Ca	%Cu	%S	%C
6	5.7	2.7	63.7	19.6	0.2	7.5	0.6	n.a.
7	3.3	2.5	60.7	19.4	0.0	13.7	0.5	n.a.
8	2.0	2.6	61.3	20.9	0.2	12.6	0.4	n.a.
9	4.9	2.8	61.9	19.4	0.1	10.2	0.6	n.a.
10	5.8	2.3	59.8	20.9	0.2	9.2	1.3	n.a.
Average	4.4	2.6	61.5	20.1	0.1	10.6	0.7	n.a.
Maximum σ	0.01	0.01	0.06	0.03	0.01	0.03	0.01	
Bulk Alloy	2.6	2.1	53.9	19.1	0.16	20.8	0.1	1.2

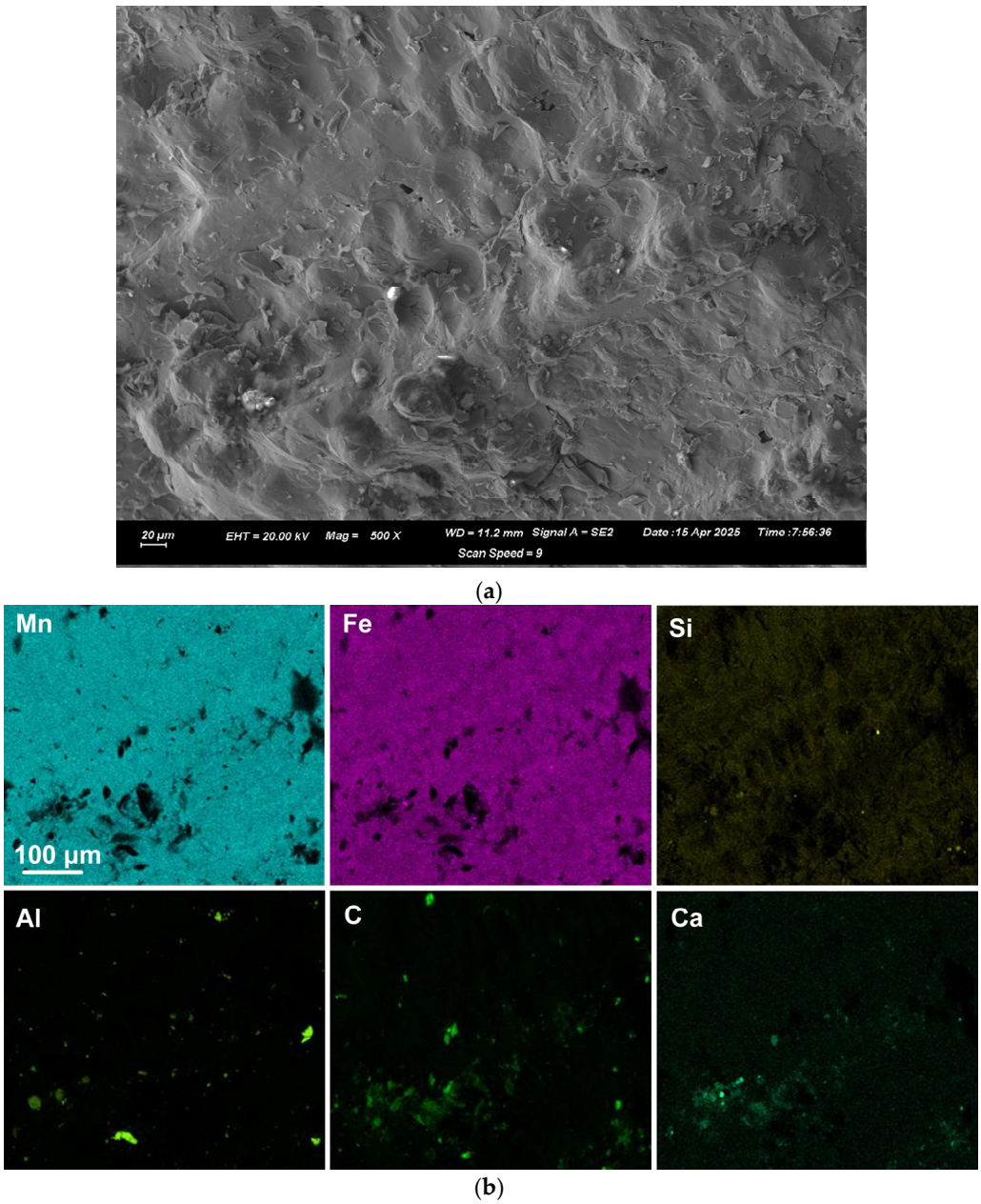

Figure 3. (**a**): SEM image (×500) of analysed area (number 3) in Sample B; (**b**): EDX map of area in (**a**).

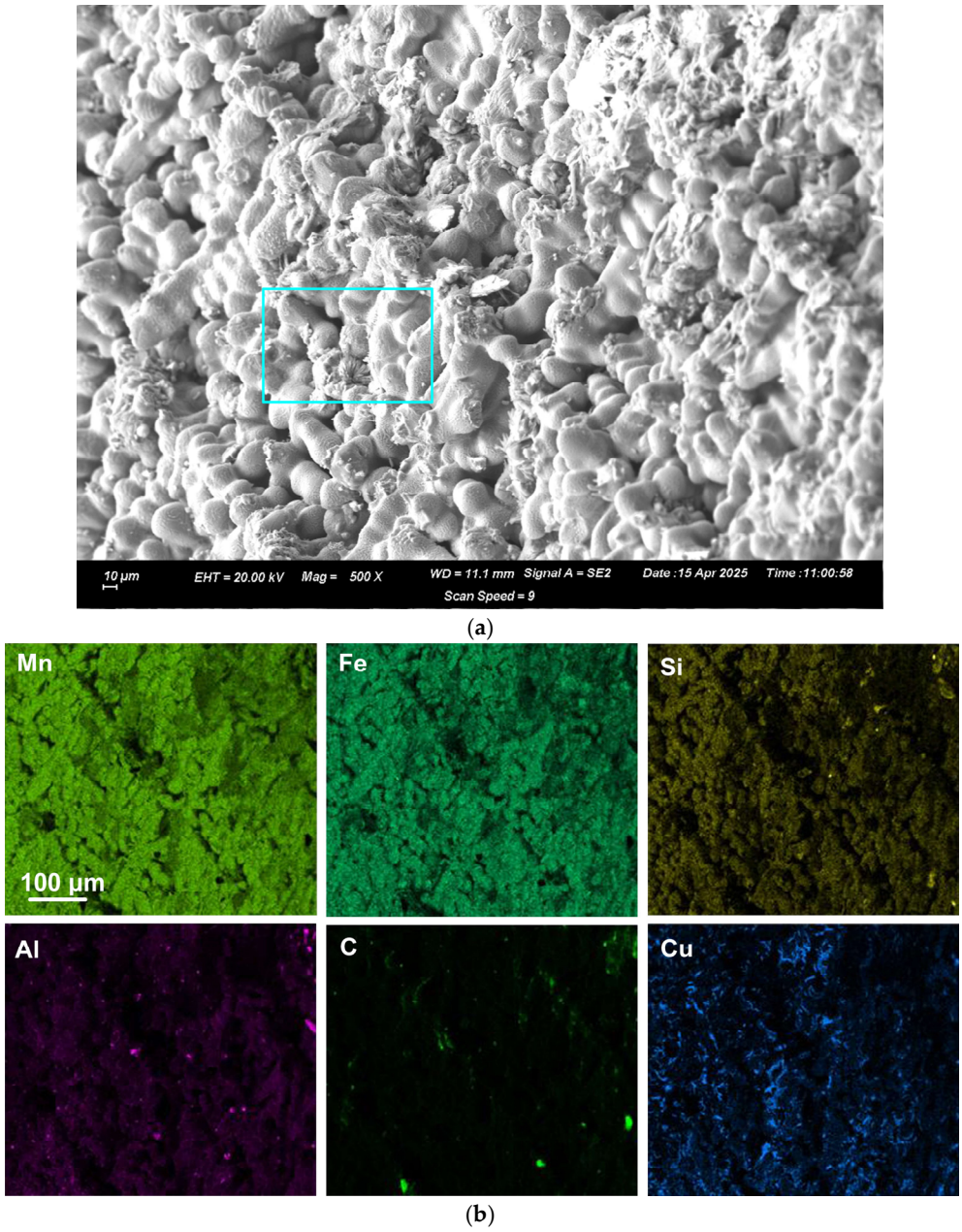

Figure 4. (**a**): SEM image (×500) of analysed area (number 10) in Sample B; (**b**): EDX map of area in (**a**).

In contrast, the Sample B alloy does not appear homogeneous, consisting of a primary alloy with a coarse dendritic structure of Mn–Fe–Si–Al and interdendritic Mn–Fe–Si–Al–Cu alloy. Consequently, variability is observed in the SEM–EDX analyses, particularly in the %Cu and %Al values. The bulk alloy chemistry and the average SEM–EDX analyses revealed significant differences, with 10.6% Cu versus 20.8% Cu, 4.4% Al versus 2.6% Al, and 61.5% Mn versus 53.9% Mn. However, the percentages of Si and Fe are similar, at 2.6% Si vs. 2.1% Si and 20.1% Fe vs. 19.1% Fe. The formation of a coarse dendritic structure in cast copper anode plates is well documented, with large grain sizes ranging from 100 to 150 µm [32]. Despite the finer dendritic structures in Figures 4 and 5, which are approximately 10 µm, the result is an undesired open-pore structure. Section 4.1 provides a detailed discussion of the likely formation pattern of the high-copper-content phase.

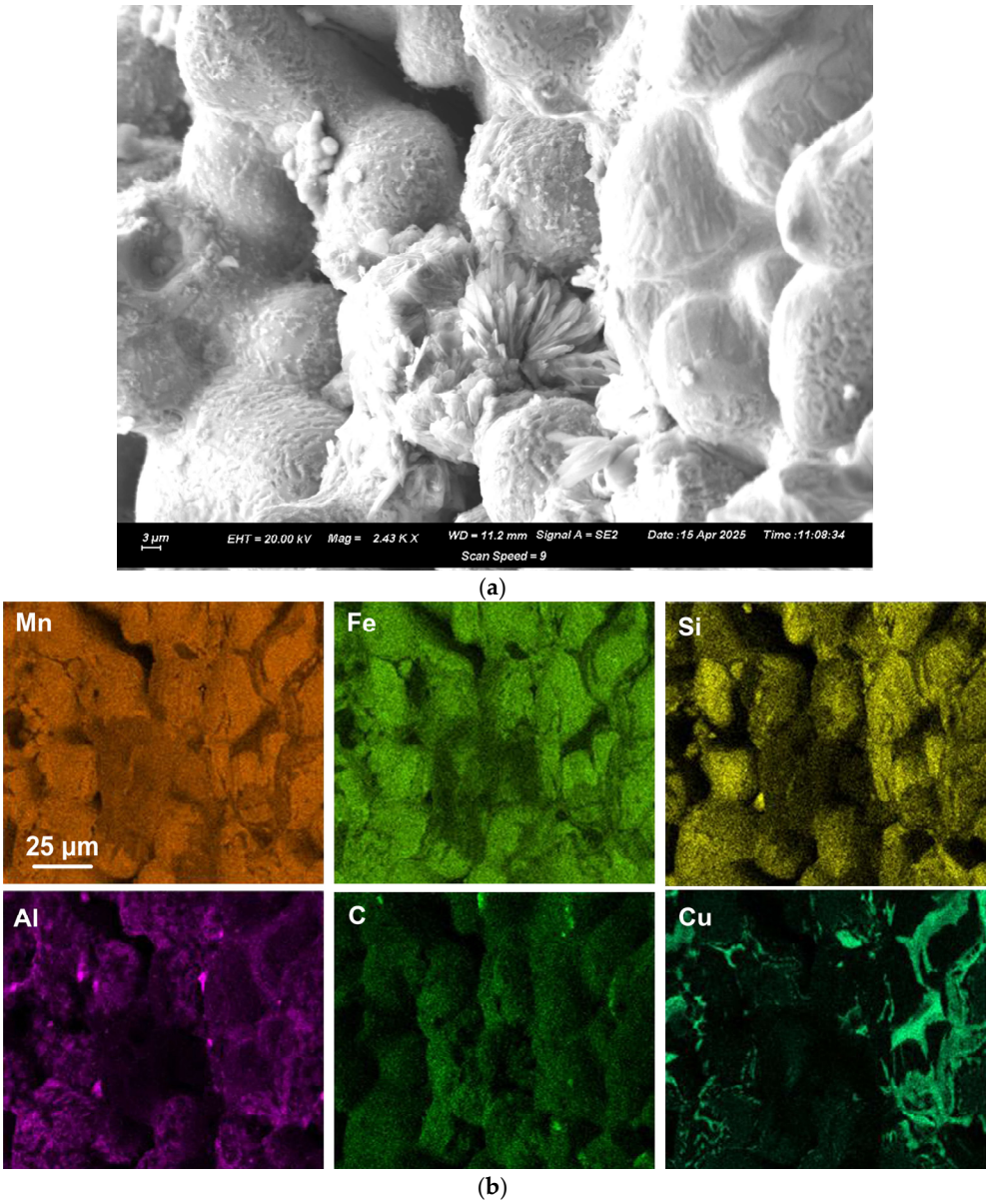

Figure 5. (**a**): SEM image (×2430) of analysed area (number 10) as marked in Figure 4a for Sample B; (**b**): EDX map of area in (**a**).

In both alloys, the same appearance of carbon as surface specs is observed. This is not the bulk carbon, which is dissolved in the alloy at 3.5% C in the Sample A alloy and 1.2% C in alloy B. The carbon specs may form from carbon deposition as CO gas dissociates upon cooling via reaction (1), the reverse Boudouard reaction.

$$2[CO] = <C> + [CO_2] \quad (1)$$

< > = solid; [ ] = gas.

Significant quantities of CO gas may form as a reduction product in the reaction of Mn and Fe oxides with coal carbon. Similarly, Al and Ca appear as specs in Figure 3 and Al in Figures 4 and 5, indicating possible evaporation and recondensation from the likely high temperatures attained in the exothermic aluminothermic reduction process. The rosette at the centre of Figure 5 contains the Mn–Fe–Si alloy, which appears to have formed from condensation in the gas phase.

4. Discussion

Even though aluminothermy processing does not reach equilibrium, equilibrium-phase calculations are useful in investigating the effects of different melting points and chemistries of the target and realised slag and alloy compositions. In the following section, the thermochemical software FactSage 7.3 and Thermo–Calc 2023b are used to calculate the equilibrium compositions for comparison with the experimental results presented in this work [27,28]. The primary reason for not attaining chemical equilibrium in aluminothermic reduction is rapid heat release, which results in short reaction times and therefore limited time for product diffusion to form homogeneous equilibrium phases [33].

4.1. Alloy Composition

The carbon saturation level for the Sample A alloy at 1550 °C is 6.5% C. In the copper-containing Sample B alloy, the 1550 °C carbon saturation level is 4.6% C for the average EDX analysis at 10.6% Cu and 3.4% C for the bulk alloy chemistry analysis at 20.8% Cu. Thus, the alloy's carbon solubility decreases with increasing %Cu [27,28]. In comparison, the bulk alloys in Tables 5 and 6 display carbon levels of 3.5% C in alloy A and 1.2% C in alloy B. The importance of these numbers is that the crucible material is graphite, and despite the excessive amount of graphite carbon available for assimilation into the alloy, the carbon dissolution process is limited by fast reaction and limited alloy–graphite contact area. This effect has been demonstrated in recent work on the aluminothermic reduction of iron oxide in graphite crucibles, producing carbon steel with a carbon content of less than 0.68% [7,8].

The equilibrium phase chemistry of the bulk alloy compositions is displayed as cooling graphs in Figure 6a,b.

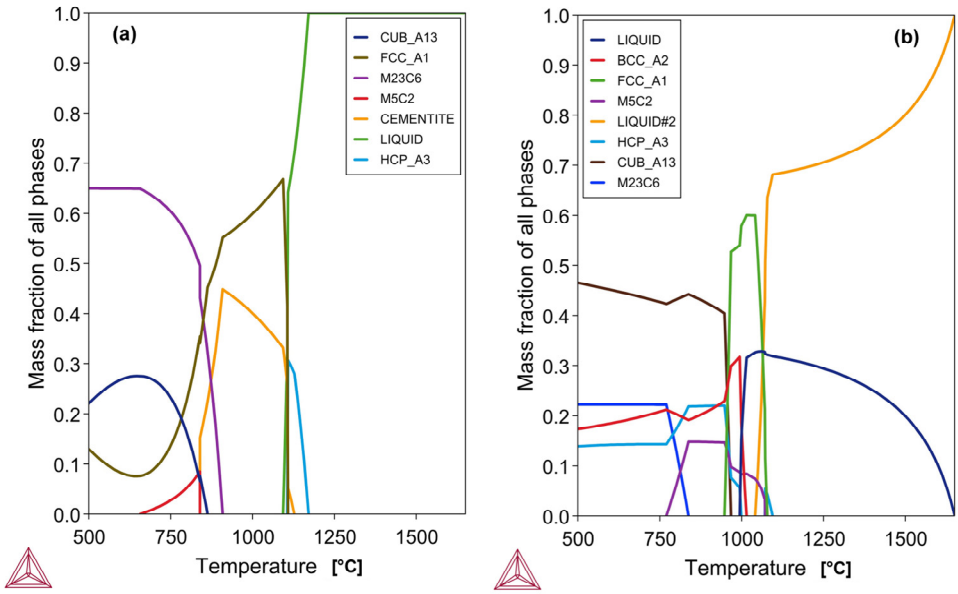

Figure 6. Phase chemistry of alloy: (**a**) Sample A alloy; (**b**) Sample B alloy. Calculated in Thermo–Calc [27].

The Sample A alloy data in Figure 6a indicate a solidus temperature of 1093 °C and a liquidus temperature of 1171 °C. In comparison, the Sample B alloy indicates a solidus temperature of 994 °C and a liquidus temperature of 1095 °C. The closeness of the solidus and liquidus temperatures results in a narrow solidification temperature range and should lead to a rapid setting of the solid alloy composition. In addition, the low liquidus and solidus temperatures, relative to the high temperatures attained in aluminothermic

reduction, which can reach 3000 °C, allowing for a longer time for the alloy beads to separate from the slag [18]. Similarly, given the large alloy superheat, it is expected that a homogeneous alloy mass would form easily. However, the alloy Sample B bulk phase chemistry in Figure 6b indicates that two liquid phases are stable above the liquidus temperature, with the Liquid#2 being phase-dominant.

At the liquidus temperature of 1095 °C, the liquid proportions are at 32% Liquid#2 and 68% Liquid phase. The proportion of the Liquid#2 phase then decreases rapidly as the first solid phase, HCP_A3, forms and, subsequently, large quantities of FCC_A1 and small amounts of M_5C_2 form. At 1041 °C, the Liquid#2 phase is at zero percent, and the Liquid phase remains. The liquid alloy chemistry of the two liquids above the solidus temperature is displayed in Figure 7. It is observed that the Liquid#2 phase is a high-Mn low-Cu phase, and the Liquid phase is the opposite, a high-Cu low-Mn phase. Therefore, it is expected that the last liquid to solidify will consist of the Liquid phase and contain a high percentage of Cu and a low percentage of Mn, with the composition of 30.2% Mn, 62.9% Cu, 4.7% Al, 1.9% Si, and negligible carbon at 0.005%. The two liquids of differing compositions may explain the interdendritic high-Cu alloy observed in Figures 4 and 5.

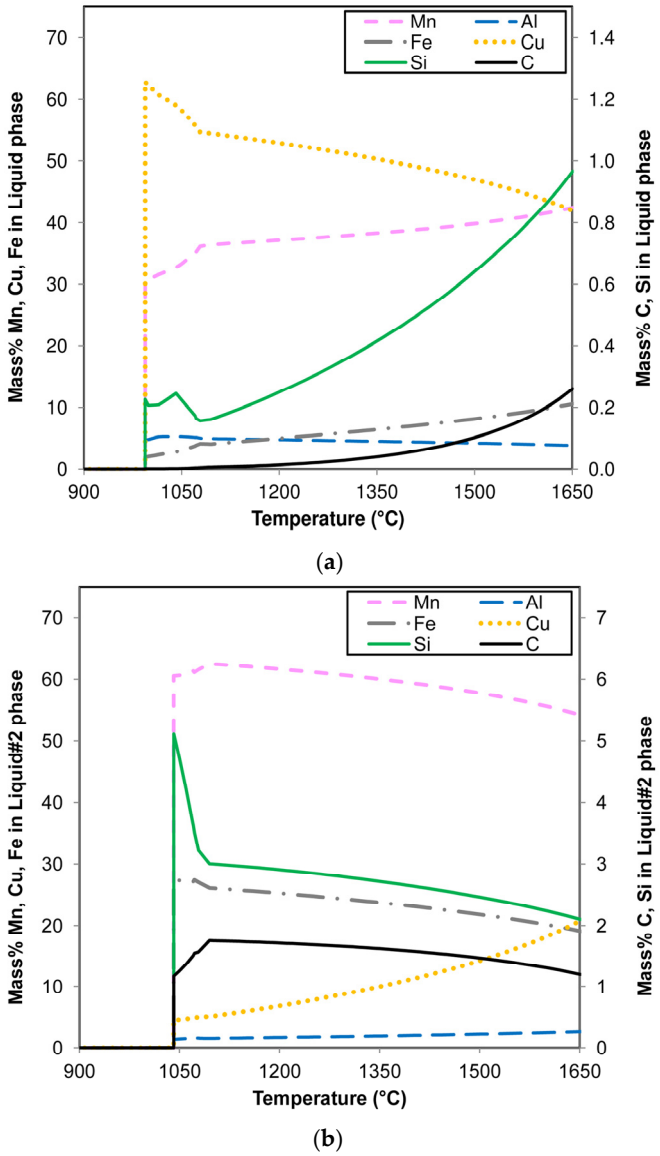

Figure 7. Sample B alloy liquids phase chemistry: (**a**) Liquid phase; (**b**) Liquid#2 phase.

4.2. Slag Composition

The slag is designed to ensure adequate slag fluidity at increasing %Al_2O_3, thereby facilitating alloy–slag separation during the process and promoting the crystallisation of the water-soluble $NaAlO_2$ phase upon solidification. The high melting point of Al_2O_3 (2072 °C) requires extreme fluxing of the slag to maintain slag fluidity upon slag cooling. Figure 8a,b shows the cooling curves of the target slag composition and the SEM–EDX average analysis of slag B (Table 7). The target slag is the expected slag composition from a simple mass balance under assumption of 100% Fe and 80% Mn recovery to the alloy. As shown in Figure 8b, the higher percentage of Al_2O_3 in slag B, 55%, leads to the formation of the spinel phase as the primary solidification phase. The slag liquidus temperature is higher at 1564 °C compared to the target slag liquidus temperature of 1373 °C. This aspect does not appear to be problematic at the high temperatures expected in aluminothermic reduction. The calculated slag viscosities of the fully liquid slags are compared in Figure 9. It is seen that the slag viscosity values are acceptable in terms of tappable slag, typically at less than 3 Poise in viscosity [34].

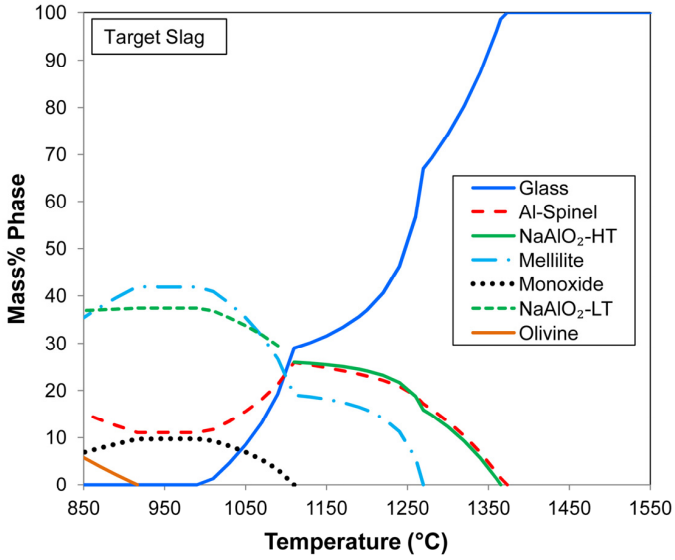

(**a**)

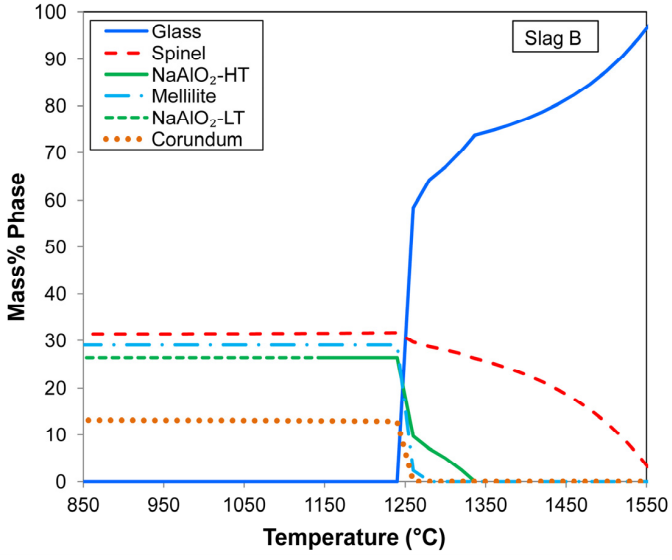

(**b**)

Figure 8. (**a**): Target slag phase chemistry. (**b**): Slag B phase chemistry.

Table 7. Target vs. experimental slag analyses (SEM Average) and bulk chemistry.

	$\%Al_2O_3$	$\%SiO_2$	%MnO	%FeO	%CaO	$\%Na_2O$	%BaO	$\%Cu_2O$	B2 = $\%CaO/\%SiO_2$
Target slag	39	17	14	0.0	17	11	2	0	1.0
A: EDX	54.5	9.1	20.0	0.0	8.0	5.5	2.8	0	0.9
A: bulk	53.2	12.3	27.6	2.4	7.1	4.6	1.5	0	0.6
A: Corrected	52.1	11.9	22.7	0.0	7.0	4.5	1.5	0	0.6
B: EDX	55.0	11.2	12.3	0.0	11.7	7.3	2.4	0	1.0
B: bulk	52.4	11.6	25.3	2.4	9.7	5.2	1.5	2.9	0.8
B: Corrected	52.3	11.4	19.4	0.0	9.8	5.2	1.5	0.0	0.9

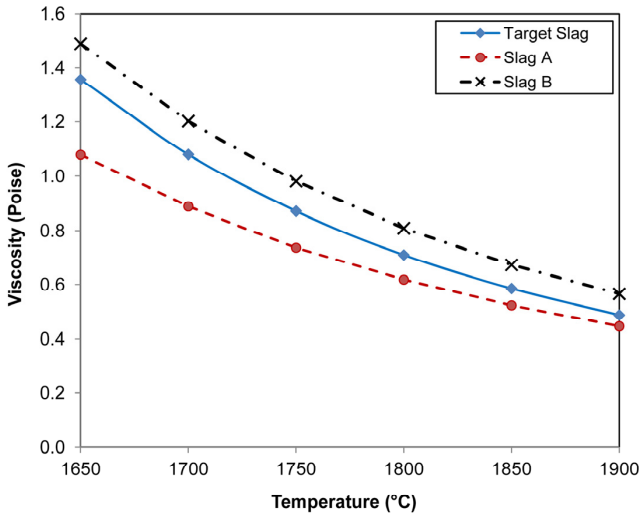

Figure 9. Calculated slag viscosity.

The difference between the average SEM–EDX slag analyses to the bulk slag analyses (Table 7) indicates that some alloy entrapment occurred in both Samples A and B, as represented by the 2.4% FeO content in the bulk slag compositions. Due to the highly reducing conditions in aluminothermic smelting, it is expected that all of the Fe oxide in the feed mixture will ultimately be reduced to Fe metal in the alloy. Similarly, the 2.9% Cu_2O in the bulk slag analysis represent an entrapped alloy in the slag since Cu is more inert to oxidation than Fe. The mass balance calculation numbers are summarised Table 8. The calculations are made as the difference between the input masses and the output masses of slag and alloy and indicate the alloy mass in the slag and the overall alloy recovery percentages. A comparison of the numbers for Sample A versus Sample B at 43% versus 57% alloy yield indicates an improvement in alloy yield with Cu added as the collector metal.

Table 8. Mass balance numbers (grams unless indicated differently).

	Alloy	Mn in Alloy	Fe in Alloy	Slag	Fe in Slag	Alloy in Slag	Mn in Ore	Fe in Ore	Mn + Fe + Cu	%Alloy Yield
A	18.7	12.4	5.3	79.1	1.5	5.3	47.7	8.3	56.0	43
B	28.6	15.4	5.5	88.5	1.7	8.8	47.7	8.3	66.0	57

The element accounting percentages shown in Table 9 indicate a good accounting of Fe and Cu, with some loss of Mn, Si, and Al to the gas. At an industrial scale, various methods of gas-cleaning and particulate-capturing equipment can be applied, for example, a reaction chamber hood with a positive off-gas pressure. Such methods counter volatilisation and

capture fumes for recycling [11]. The differences between the SEM–EDX slag analyses and the target slag analysis in Table 7 are lower percentages of CaO and Na_2O and higher levels of Al_2O_3, obtained in the experimental results. The composition differences between the experimentally attained slags and the target slag can be overcome by adding Na_2O flux to the post-tapped slag to increase the proportion of the water-soluble $NaAlO_2$ phase. As discussed in [9], the high-residual-heat content remains after the aluminothermic reaction, and this heat should be utilised to incorporate more Na_2O Flux into the tapped slag.

Table 9. Mass accounting of primary elements (percent).

	%Fe	%Mn	%Si	%Al	%Cu
Sample A	81	67	58	62	none
Sample B	86	72	64	69	82

4.3. Gas–Slag–Metal Equilibrium Thermochemistry

The gas–slag–metal equilibrium for the feed mixture inputs was calculated at temperatures of 1650 °C–1900 °C. The calculated equilibrium end-point alloy and slag analyses for Samples A and B are compared to the experimentally determined values, as shown in Figure 10a–d.

The alloy composition data in Figure 10a,b show that the Sample A carbon content line at 3.5% C crosses the equilibrium curve at 1650–1700 °C, even though the equilibrium %C range is broad (0.5–3.9% C at 1650 °C–1900 °C). The Sample B carbon content line at 1.2% C crosses the equilibrium curve at 1700 °C–1750 °C and the carbon range is narrower (0.2–2.1% C) compared to the %C range in Sample A (0.5–3.9% C). Therefore, it appears that the Cu collector metal modulates the alloy's carbon content. This is expected, as the solubility of carbon in copper is zero at temperatures up to 2000 °C [27,28]. The solubility of carbon in manganese is lowered with the addition of copper to manganese [35].

The Sample A silicon content line at 1.4% Si crosses the equilibrium curve at 1650–1700 °C, in agreement with the carbon equilibrium temperature. The %Si for the Sample B alloy at 1.2% Si crosses the equilibrium curve at 1700 °C. Both %C and %Si equilibrium contents vary broadly across the temperature range of 1650 °C–1900 °C. In particular, the %Si range is wide, spanning from 1.1% Si to 6.4% Si in Sample A and from 1.5% Si to 4.6% Si in Sample B. The %Al in the alloy is under-predicted for both Sample A and B alloys, with 0.4% Al in alloy A compared to only 0.02–0.12% Al predicted over the 1650–1900 °C temperature range. The %Al in the Sample B alloy is significantly higher than in the Sample A alloy at 2.6% Al, compared to the equilibrium range of 0.03–0.17% Al. These numbers indicate that the equilibrium calculation does not correspond to the experimental observations regarding the extent of Al reaction. However, the %C and %Si levels appear to be indicators of the trends, as there is an overlap of values, and these are all undersaturated in carbon.

The %Mn and %Fe equilibrium values at 1900 °C are the closest to the experimental values for both alloys. The equilibrium value range is from 68% Mn to 76% Mn compared to 66% in the Sample A alloy, and the equilibrium range is from 54% Mn to 66% Mn compared to 54% Mn in Sample B alloy. The alloy B copper content at 1900 °C equilibrium is 20% Cu compared to 21% Cu analysed in the alloy. The discrepancy in the best fit equilibrium temperatures of from 1650 to 1700 °C for %C and %Si vs. 1900 °C for the closest values in %Mn and %Fe for Sample A indicates that complete equilibrium is not attained in the short reaction time of the aluminothermic reaction applied in this work. In particular, the %Al is predicted to be close to zero at equilibrium, whilst this is not the case in the produced alloy.

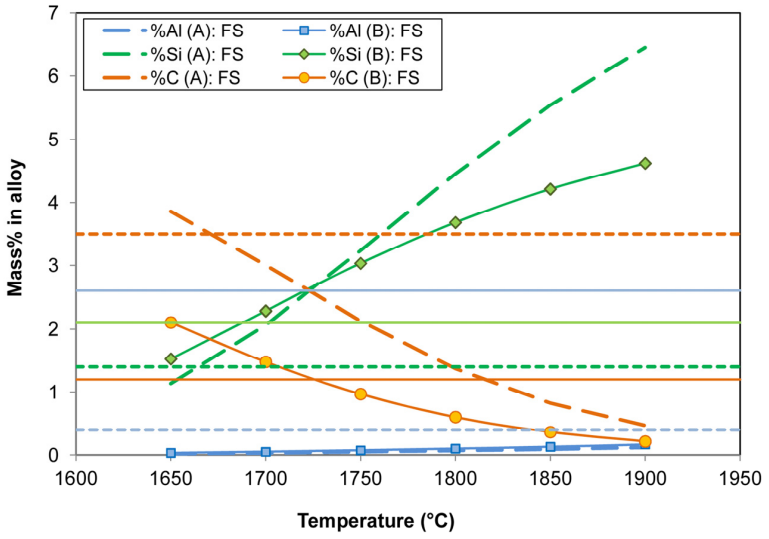

(**a**)

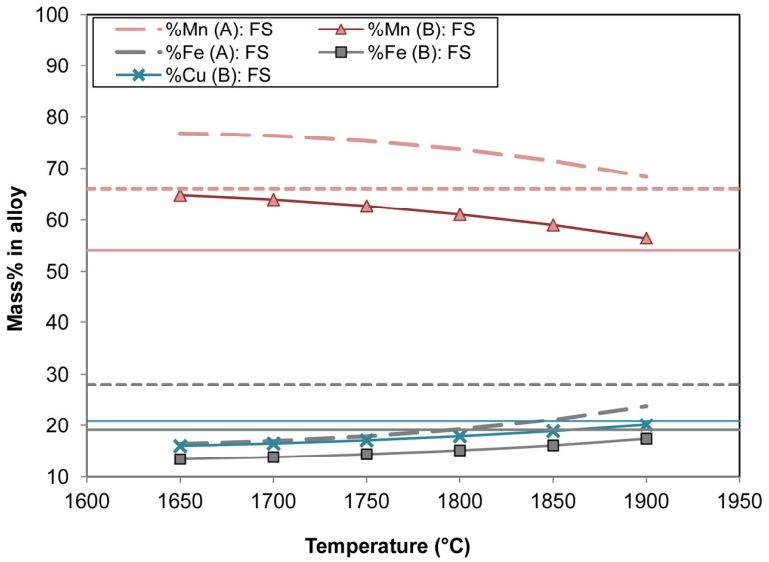

(**b**)

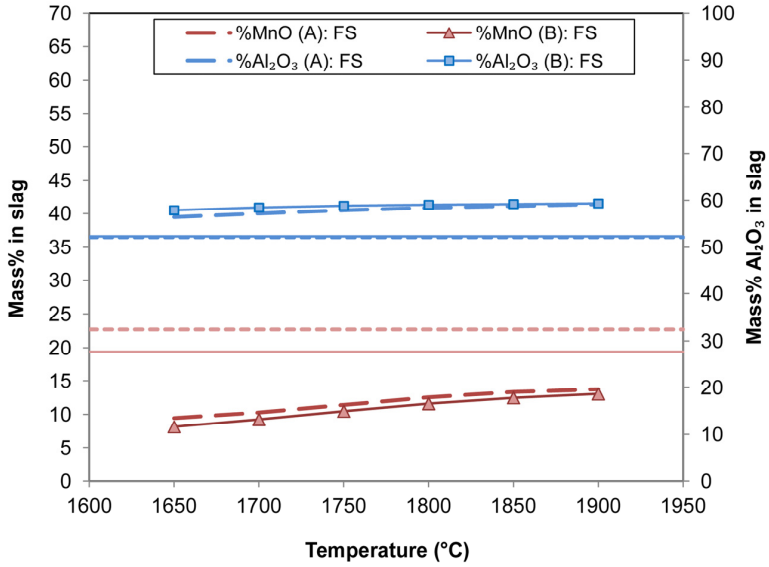

(**c**)

Figure 10. *Cont*.

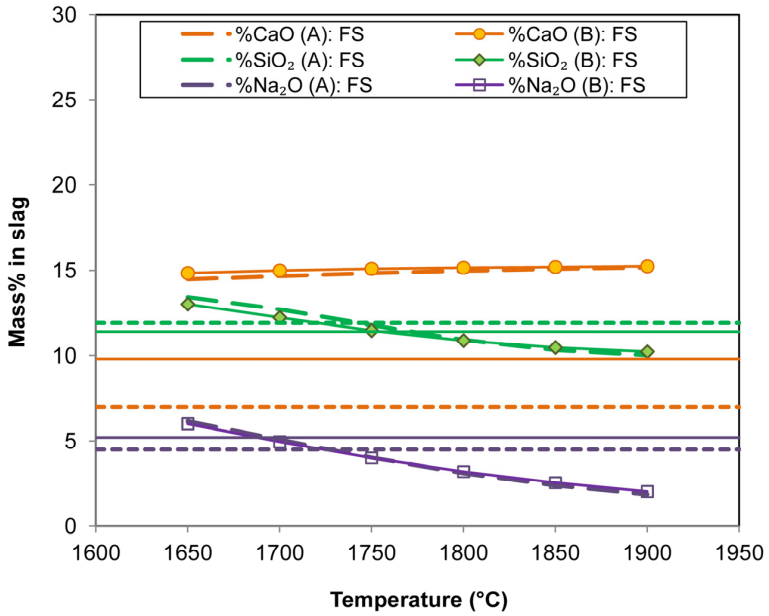

(**d**)

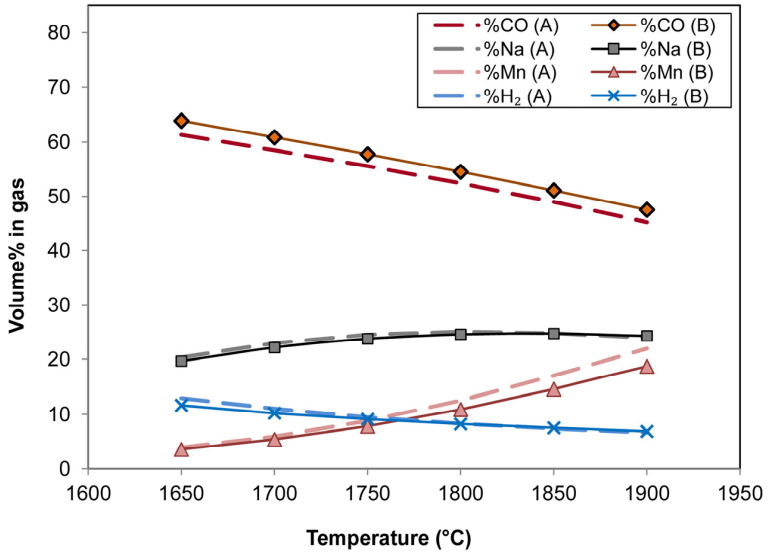

(**e**)

Figure 10. Composition of Samples A and B vs. gas–slag–metal equilibrium (FS = FactSage) (**a**): Alloy (minor elements). (**b**): Alloy (major elements). (**c**): Slag (major elements) (**d**): Slag (minor elements). Horizontal lines indicate bulk alloy and slag chemistry in Tables 5–7, Sample A (dotted lines) and B (complete lines). (**e**): Gas composition.

Figure 10c,d displays the slag compositions in comparison to the equilibrium lines at 1650–1900 °C. The equilibrium lines for Sample A and Sample B slag are the same since the copper metal added in Sample B is inert with respect to the slag components. It is seen that the $\%Al_2O_3$ in slag A and slag B are the same at 52%, compared to the higher values predicted for equilibrium at 56–59% Al_2O_3. This discrepancy arises from the complete oxidation of Al predicted in the equilibrium calculations, compared to some Al remaining in reserve in the alloy. Higher levels of MnO in the slags at 22.7% MnO in slag A and 19.4% MnO in slag B, compared to the equilibrium values of 8%–13%, indicate lower Mn recovery in the experiments. The slag A and slag B %CaO are lower than the equilibrium values, possibly due to the incomplete incorporation of CaO into the melt. The SiO_2 and Na_2O contents in the slags correspond to the equilibrium values at temperatures ranging from

1700 to 1750 °C. The equilibrium gas compositions for Samples A and B are similar, as displayed in Figure 10e. The gas consists of CO, Na, Mn, and H_2. Little Cu is present in the Sample B gas composition, indicating a high distribution of Cu to the alloy as found experimentally.

The FactSage-calculated gas–slag–metal mass distribution of the elements Mn, Si, Al, and Cu for Sample B is summarised in Figure 11a–d as a function of temperature, and the element distribution of Mn, Si, and Al for Sample A are shown in Figure 12a–c. It is observed that losses of Mn and Cu to the gas phase increase with increasing temperature. Manganese has a high vapour pressure and is expected to easily enter the gas phase, as confirmed in Figure 10e. Interestingly, this trend is not seen in the case of Al, although one may expect the same behaviour from both Cu and Al, since these metals both have similar vapour pressures, even though it is orders of magnitude less than that of Mn [36,37]. Instead, Al is fully reacted in the aluminothermic reaction of MnO and SiO_2 to form Al_2O_3.

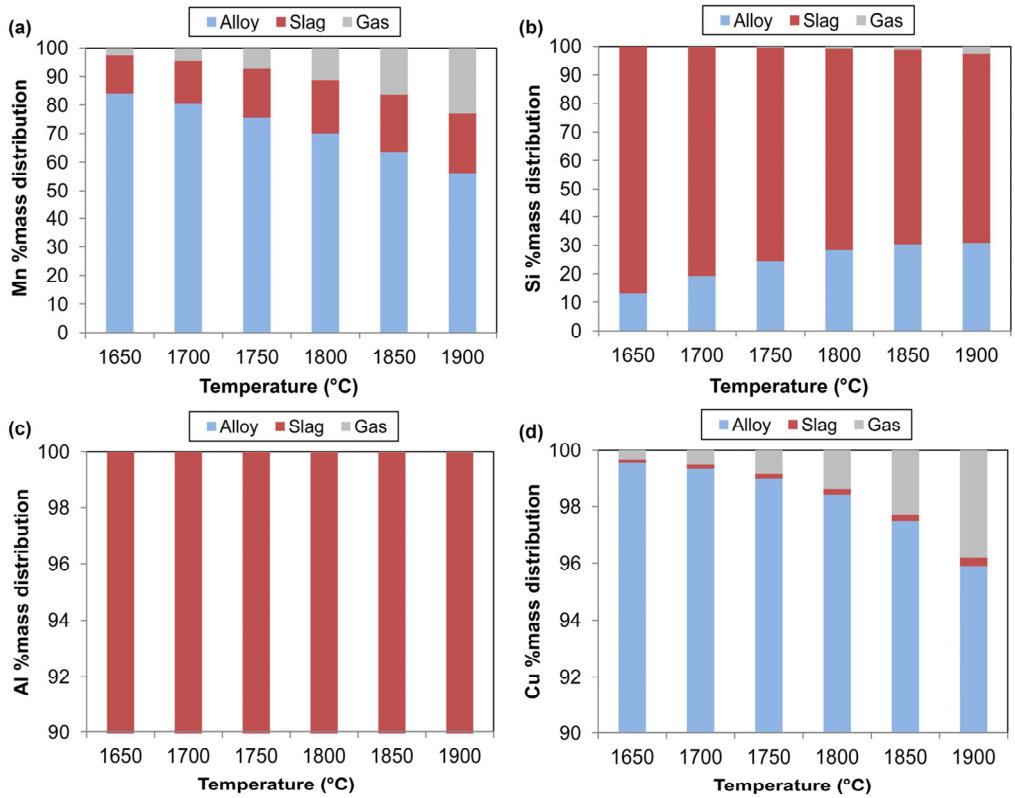

Figure 11. Element mass distribution among phases from gas–slag–metal equilibrium calculation: (**a**) Mn; (**b**) Si; (**c**) Al; (**d**) Cu in Sample B.

Copper distribution to the alloy is high, being 100% at 1650 °C and 96% at 1900 °C, with an increased loss to the gas phase as the temperature increases. Since Cu is inert to oxidation, there is no oxidation loss to the slag phase. Comparing Figure 11a to Figure 12a reveals increased the Mn recovery of 2–6% to the alloy in Sample B with added Cu. Comparing Figure 11b to Figure 12b shows a higher distribution of Si to the alloy in Sample B (by 3–5%) at 1650 °C compared to 1700 °C.

The only difference between the Sample A and B inputs is the addition of the Cu collector metal. The output slag analyses are similar. Therefore, the effect of Cu on the activity of the Mn alloy is considered. Figure 13a,b shows the equilibrium activities in the bulk alloy products. The main difference is the lowered activity of Mn in Sample B due to the addition of Cu. According to Le Chatelier's principle, lowering the Mn activity will increase the driving force of reaction (2) towards completion [11]. At the start of the

aluminothermic reduction process, the activity differences in Mn in the alloy of Sample A and Sample B would be greater because the initial alloy formation consists of much Cu and little Mn in Sample B, compared to mostly Mn in Sample A alloy.

$$3\langle MnO\rangle + 2(Al) = \langle Al_2O_3\rangle + 3(Mn) \quad (2)$$

< > = solid; ( ) = liquid.

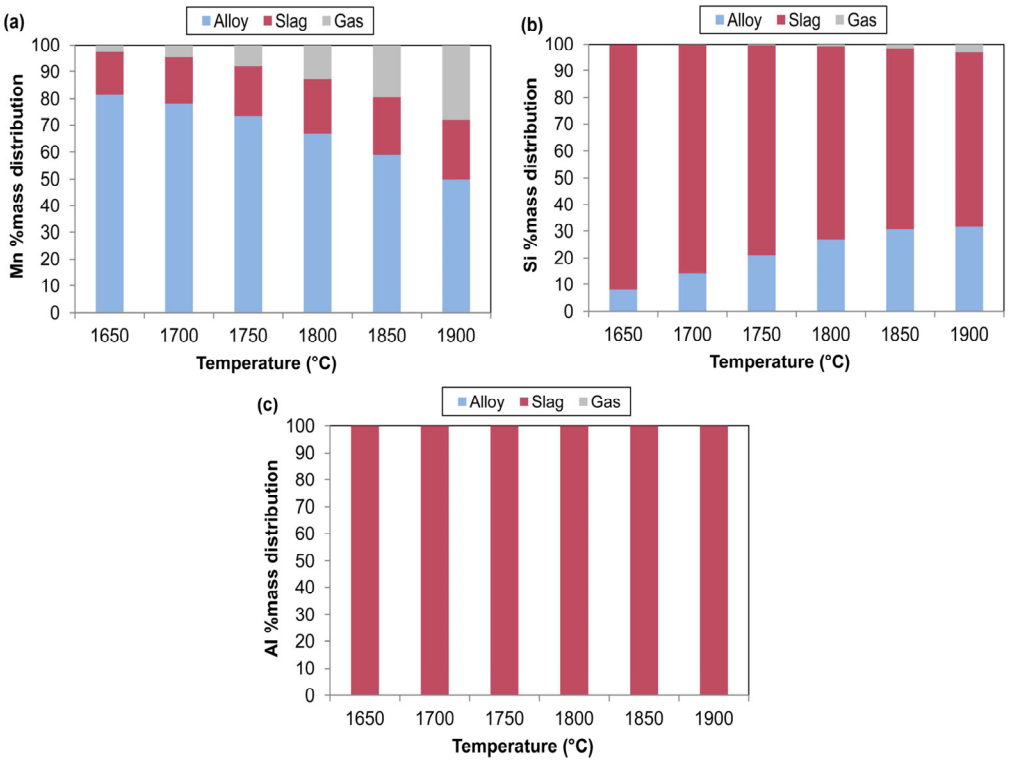

Figure 12. Element mass distribution among phases from gas–slag–metal equilibrium calculation: (**a**) Mn; (**b**) Si; (**c**) Al in Sample A.

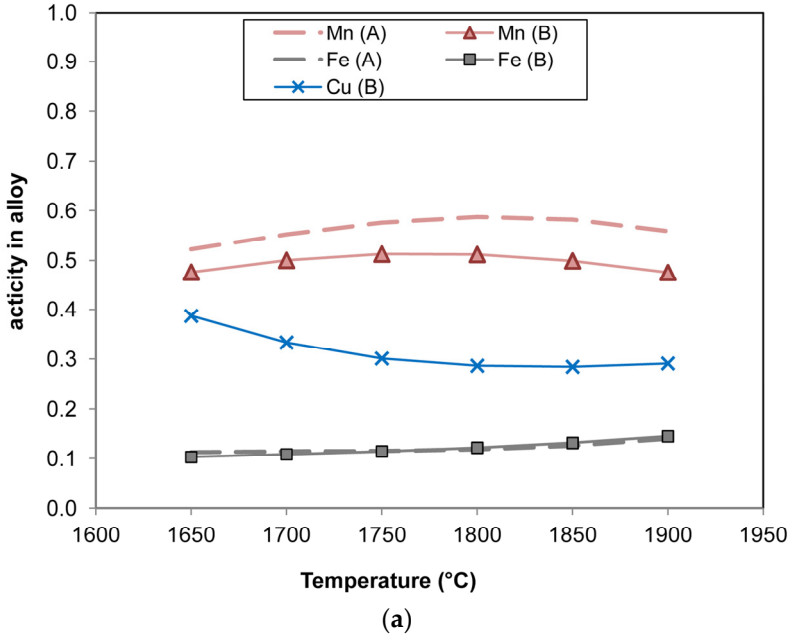

(**a**)

Figure 13. *Cont.*

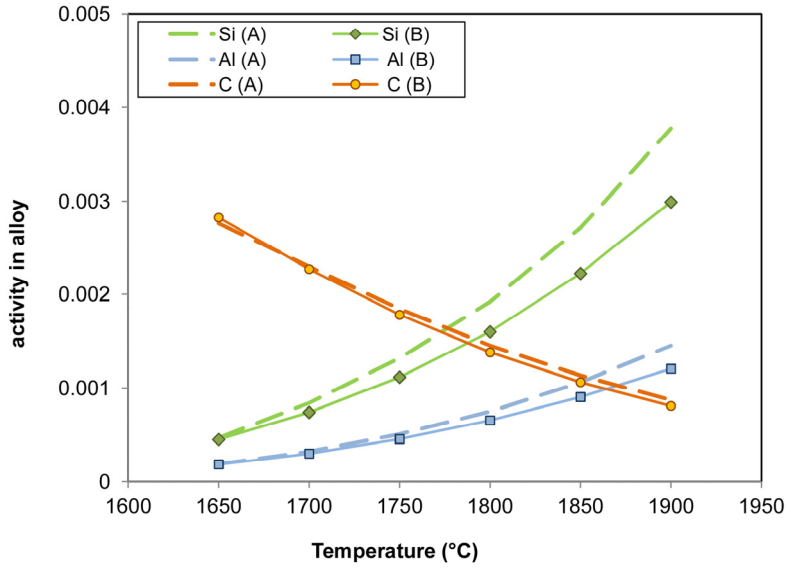

(**b**)

Figure 13. Element activities in alloy phase: (**a**) Mn, Fe, Cu; (**b**) Si, Al, C.

The fact that aluminium particle size strongly influences the overall aluminothermy reaction extent implies that the aluminium reduction reaction is controlled at the aluminium oxide reaction interface [33,38,39]. This effect is the analogue of MnO in slag reduced by carbon, with the reaction interface area as the main unknown [40]. The driving force for the chemical reaction is the MnO activity in the slag relative to its equilibrium value. The MnO_2 ore has few fluxing compounds (Table 3), resulting in high MnO activity at the start of reduction via reaction (2). Similarly, the aluminium particles should be pure at the start of reduction. The formation of an Al_2O_3 product film on the surface of aluminium particles was shown in previous work, but this film was not continuous and its breakup occurred easily [41]. In the aluminothermy of SiO_2–MnO–Fe–Al mixtures, a ferrosilicomanganese powder product was formed with some Al_2O_3 particles entrapped in the alloy phase, even though both the oxide and alloy were reported as molten [42]. The application of fluxing agents in the current study should improve the separation of the Al_2O_3 product from the alloy, and as the fluxes dissolve Al_2O_3 at the reaction interface, the Al_2O_3 activity is lowered to drive reaction (2) towards completion. The sequence of the melting of reactants and products can influence the reaction rate. Since aluminium has a low melting point of 660 °C compared to copper at 1083 °C, manganese at 1244 °C, silicon at 1410 °C, and iron at 1535 °C, it is expected that aluminium melts before its reaction with the oxides. The reaction of liquid aluminium was observed in the reaction of aluminium with MgO, in which the reduction in MgO proceeded after the molten aluminium covered the MgO [41]. Therefore, in addition to optimising the chemistry design to maximise reactant activities and minimise product activities, thereby driving reactions to completion according to Le Chatelier's principle, the chemistry application may also be used to limit Al_2O_3 product layer formation at the reaction interface.

In addition to reaction (2) as the main reaction of importance, the following reactions are likely at play in the reaction system, as designed in this work. At low temperatures, the ore is decomposed to Fe_2O_3 and Mn_2O_3 according to reaction (3) at 680 °C and reaction (4) at 546 °C to 600 °C [43,44]. The released water and oxygen from reactions (3) and (4) can react with carbon and aluminium via reactions (5) to (8). The reaction of aluminium with the oxygen from rection (4) serves as the ignition start. The presence of reductant carbon is aimed at a reduction in Fe_2O_3 and Mn_2O_3 to FeO and MnO in reactions (9) and (10) to remove the requirement of pre-roasting, as mentioned by Bhoi et al. [1]. CO gas is

released and helps to maintain reducing conditions in the reaction volume. Aluminothermic reduction in FeO and part-reduction in SiO_2 occurs via reactions (11) and (12).

$$<FeO(OH)_2> = 1/2<Fe_2O_3> + 1/2[H_2O] \quad (3)$$

$$<MnO_2> = 1/2<Mn_2O_3> + 1/4[O_2] \quad (4)$$

$$3[H_2O] + 2(Al) = <Al_2O_3> + 3[H_2] \quad (5)$$

$$3[O_2] + 2(Al) = 2<Al_2O_3> \quad (6)$$

$$[H_2O] + <C> = [H_2] + [CO] \quad (7)$$

$$[O_2] + 2<C> = 2[CO] \quad (8)$$

$$<Mn_2O_3> + <C> = 2<MnO> + [CO] \quad (9)$$

$$<Fe_2O_3> + <C> = 2(FeO) + [CO] \quad (10)$$

$$3<SiO_2> + 4(Al) = 3(Si) + 2<Al_2O_3> \quad (11)$$

$$3(FeO) + 2(Al) = <Al_2O_3> + 3(Fe) \quad (12)$$

< > = solid; ( ) = liquid; [ ] = gas.

Considering the similarities between Sample A and B feed mixtures, and the only difference as the Cu collector metal added, it is clear that the increase in alloy yield from 43% to 57% in Sample A versus Sample B (Table 8) is mainly due to the inert Cu collector metal. The increase in the Mn yield is 6%, which is a combination of the activity-lowering effect, as shown in Figure 13a, and the collector metal effect, namely that copper droplets serve as physical collector volumes for the newly formed Mn metal via reaction (2).

In summary, this work demonstrates that a sodium-fluxed slag with high Al_2O_3 solubility can be utilised in the aluminothermic reduction in MnO_2 ore using Cu as a collector metal and adding a minor carbon reductant quantity. The addition of a carbon reductant negates MnO_2 ore pre-roasting step. The Cu collector metal increases the Mn recovery to the alloy by 6%. The feed mixture formulation yields a $NaAlO_2$-containing slag suitable for leaching to recover aluminium for circular processing, thereby providing a feed to the Hall–Héroult electrochemical process. A medium-carbon Fe–Mn–Si–Al–Cu complex ferroalloy is formed, which is suitable as a ferroalloying additive in steelmaking.

5. Conclusions

Single-step aluminothermy of MnO_2-type ore is demonstrated by adding a small quantity of carbon reductant. Thus, the need for the extra step of pre-roasting the MnO_2 ore is removed.

The added copper metal serves as a collector metal, increasing Mn recovery to the alloy by 6%. The overall alloy yield increased from 43% to 57%. The product alloy is a medium-carbon complex ferroalloy comprising 54% Mn, 19% Fe, 2.1% Si, 2.6% Al, 21% Cu, and 1.2% C, which can be applied as an efficient ferroalloying addition in steelmaking.

The feed mixture formulation based on Na_2O flux enables the crystallisation of the water-soluble $NaAlO_2$ compound, allowing for the recycling of Al_2O_3 through hydrometallurgical processing via the Bayer process to the Hall–Héroult electrochemical process, which is used to produce aluminium.

Thermochemistry calculations provide temperature estimates and trends in chemical changes, but do not accurately predict the Al requirement in the feed mixture. Therefore, theoretical feed mixture formulations must be tested using empirical applications, as shown in this work.

Author Contributions: F.D.B. provided the initial concept of the work. F.D.B. and T.C. are responsible for all the work in this manuscript. T.C. and F.D.B. All authors have read and agreed to the published version of the manuscript.

Funding: This work was supported in part by the University of Pretoria.

Data Availability Statement: The original contributions presented in this study are included in the article. Further inquiries can be directed to the corresponding author.

Acknowledgments: Gratitude to Coenraad Snyman at the Laboratory for Microscopy and Microanalysis at the University of Pretoria for his advice and assistance on SEM work.

Conflicts of Interest: The authors declare no conflicts of interest. The funders had no role in the design of the study; in the collection, analyses, or interpretation of data; in the writing of the manuscript, or in the decision to publish the results.

Abbreviations

The following abbreviations are used in this manuscript:

FCAW–S	Self-shielded fluxed-cored arc welding
HCFeMn	High-carbon ferromanganese
MCFeMn	Medium-carbon ferromanganese
LCFeMn	Low-carbon ferromanganese
SHS	Self-propagating high-temperature synthesis
AMS	Aluminium–silicon–manganese
FMA	Ferromanganese–aluminium
FAMS	Ferrosilicon–manganese–aluminium
PID	Proportional–integral–derivative
SEM	Scanning electron microscope
EDX	Energy dispersive X-ray spectroscopy
ICP–OES	Inductively coupled plasma optical emission spectroscopy
XRF	X-ray fluorescence

References

1. Bhoi, B.; Murthy, B.V.R.; Datta, P.; Rajeev; Jouhari, A.K. Studies on Aluminothermic Reduction of Manganese ore for Ferro Manganese Making. In *Proceeding: Ferro Alloy Industries in the Liberalised Economy*; Vatsh, A.K., Singh, S.D., Goswami, N.G., Ramachandrarao, P., Eds.; NML: Jainshedpur, India, 1997; pp. 66–70.
2. Kudyba, A.; Akhtar, S.; Johansen, I.; Safarian, J. Aluminothermic Reduction of Manganese Oxide from Selected MnO–Containing Slags. *Materials* **2021**, *14*, 356. [CrossRef]
3. Kudyba, A.; Safarian, J. Manganese and Aluminium Recovery from Ferromanganese Slag and Al White Dross by a High Temperature Smelting–Reduction Process. *Materials* **2022**, *15*, 405. [CrossRef]
4. Azof, F.I.; Safarian, J. Leaching kinetics and mechanism of slag produced from smelting–reduction of bauxite for alumina recovery. *Hydrometallurgy* **2020**, *195*, 105388. [CrossRef]
5. Pilla, G.; Hertel, T.; Pontikes, Y. Toward an integrated and sustainable Bauxite residue valorization, employing H_2 reduction roasting, carbonation, and bio–carbon smelting. *J. Sustain. Metall.* **2025**, *11*, 1745–1765. [CrossRef]
6. Nababan, D.C.; Mukhlis, R.; Durandet, Y.; Prentice, L.H.; Rickard, W.D.A.; Pownceby, M.I.; Rhamdani, M.A. Recycling of $LiCoO_2$ Battery Cathode Material Through Aluminothermic Reduction Using Aluminum Waste Chips. *Met. Mater. Trans. B* **2024**, *55*, 144–167. [CrossRef]
7. Barsukova, N.V.; Popov, A.V.; Komarov, O.N. Evolution of structure and properties of iron–carbon alloys produced by aluminothermy at differentiation of fractional composition of charge materials. *Metallurgist* **2025**, *68*, 1743–1755. [CrossRef]
8. Barsukova, N.V.; Komarov, O.N.; Zhilin, S.G.; Predein, V.V.; Popov, A.V.; Khudyakova, V.A. Control of Properties of Iron–Carbon Alloys Produced by Aluminothermy by Varying Technological Factors. *Metallurgist* **2023**, *67*, 1192–1207. [CrossRef]
9. Coetsee, T.; De Bruin, F. Sodium Oxide–Fluxed Aluminothermic Reduction of Manganese Ore with Synergistic Effects of C and Si Reductants: SEM Study and Phase Stability Calculations. *Reactions* **2025**, *6*, 40. [CrossRef]
10. Coetsee, T.; De Bruin, F. Sodium–Oxide Fluxed Aluminothermic Reduction of Manganese Ore for a Circular Economy: Cr Collector Metal Application. *Sustain. Chem.* **2025**, *6*, 30. [CrossRef]

11. Gasik, M. *Handbook of Ferroalloys*; Butterworth–Heinemann: Oxford, UK, 2013; pp. 495–499.
12. Zhuniskaliyev, T.; Nurumgaliyev, A.; Chekimbayev, A.; Kelamanov, B.; Kuatbay, Y.; Mukhambetgaliyev, Y.; Mukhambetkaliyev, A.; Abdirashit, A. Experimental Investigation of the Influence of Phase Compounds on the Friability of Fe–Si–Mn–Al Complex Alloy. *Metals* **2024**, *14*, 1091. [CrossRef]
13. *ASTM A99–03*; Standard Specification for Ferromanganese. ASTM International: West Conshohocken, PA, USA, 2014.
14. Habashi, F. (Ed.) *Handbook of Extractive Metallurgy*; Wiley–VCH: Weinheim, Germany, 1997; Volume 1, pp. 420–451.
15. Makhambetov, Y.; Abdulina, S.; Kabylkanov, S.; Burumbayev, A.; Zhakan, A.; Sadyk, Z.; Akhmetov, A. Production of Chromium–Manganese Ligature from Low–Grade Chromium and Iron–Manganese Ores Using Silicon–Aluminum Alloys as Reductants. *Processes* **2025**, *13*, 3158. [CrossRef]
16. Andrusev, M.M. 150 Years since the birth of the eminent Russian physical chemist and metallurgist N.N. Beketov. *Metallurgist* **1977**, *21*, 416–418. [CrossRef]
17. Sarangi, B.; Sarangi, A.; Ray, H.S. Kinetics of aluminothermic reduction of MnO_2 and Fe_2O_3: A thermoanalytical investigation. *ISIJ Int.* **1996**, *36*, 1135–1141. [CrossRef]
18. Branzei, M.; Cojocaru, M.O.; Coman, T.A.; Vascan, O. A model of optimization and control the thermite kit for aluminothermic welding. *Solid State Phenom.* **2016**, *254*, 83–90. [CrossRef]
19. Trembach, B.; Grin, A.; Makarenko, N.; Zharikov, S.; Trembach, I.; Markov, O. Influence of the core filler composition on the recovery of alloying elements during the self–shielded flux–cored arc welding. *J. Mater. Res. Technol.* **2020**, *9*, 10520–10528. [CrossRef]
20. Trembach, B.; Trembach, I.; Grin, A.; Makarenko, N.; Babych, O.; Knyazev, S.; Musairova, Y.; Krbata, M.; Balenko, O.; Vorobiov, O.; et al. Study of the Effects of Hardfacing Modes Carried out by FCAW–S with Exothermic Addition of MnO_2–Al on Non–Metallic Inclusions, Grain Size, Microstructure and Mechanical Properties. *Eng* **2025**, *6*, 125. [CrossRef]
21. Park, Y.D.; Kang, N.; Malene, S.H.; Olson, D.L. Effect of exothermic additions on heat generation and Arc process efficiency in Flux–Cored Arc welding. *Met. Mater. Int.* **2007**, *13*, 501–509. [CrossRef]
22. De, S.K.; Srikanth, S.; Saxena, A.K.; Jha, B.K. Copper bearing steels from SAIL and its application. *Int. J. Metall. Eng.* **2016**, *5*, 1–8.
23. Sharma, K.D.; Mandal, A.; Sarkar, A.; Trivedi, R.; Hasan, S.M.; Patra, S.; Karmakar, A. Tailoring the microstructural characteristics for enhancing the wear performance of Cu–based low–carbon steel. *Met. Mater. Trans. A* **2025**, *56*, 3309–3327. [CrossRef]
24. Lozynskyi, V.; Trembach, B.; Katinas, E.; Sadovyi, K.; Krbata, M.; Balenko, O.; Krasnoshapka, I.; Rebrova, O.; Knyazev, S.; Kabatskyi, O.; et al. Effect of Exothermic Additions in Core Filler on Arc Stability and Microstructure during Self–Shielded, Flux–Cored Arc Welding. *Crystals* **2024**, *14*, 335. [CrossRef]
25. Mandal, S.; Kishore, V.; Bose, M.; Nandi, S.K.; Roy, M. In vitro and in vivo degradability, biocompatibility and antimicrobial characteristics of Cu added iron–manganese alloy. *J. Mater. Sci. Technol.* **2021**, *84*, 159–172. [CrossRef]
26. *SANS 17246:2011; ISO 17246:2010*; South African National Standard Coal–Proximate Analysis. SABS Standards Division: Pretoria, South Africa, 2011.
27. Andersson, J.–O.; Helander, T.; Höglund, L.; Shi, P.; Sundman, B. Thermo–Calc & DICTRA, computational tools for materials science. *Calphad* **2002**, *26*, 273–312. [CrossRef]
28. Bale, C.W.; Bélisle, E.; Chartrand, P.; Decterov, S.A.; Eriksson, G.; Gheribi, A.E.; Hack, K.; Jung, I.-H.; Kang, Y.-B.; Melançon, J.; et al. FactSage thermochemical software and databases, 2010–2016. *Calphad* **2016**, *54*, 35–53, Reprinted in *Calphad* **2016**, *55*, 1–19.
29. Braga, R.S.; Takano, C.; Mourao, M.B. Prereduction of self–reducing pellets of manganese ore. *Ironmak. Steelmak.* **2007**, *34*, 279–284. [CrossRef]
30. Akdogan, G.; Eric, R.H. Kinetics of the solid–state carbothermic reduction of Wessel manganese ores. *Metall. Mater. Trans. B* **1995**, *26*, 13–24. [CrossRef]
31. Coetsee, T. The Role of Metallic Iron in Low Temperature Carbothermic Reduction of MnO: Phase Chemistry and Thermodynamic Analysis. *Minerals* **2021**, *11*, 1205. [CrossRef]
32. Morales–Aragon, A.; Sánchez–Rodas, D.; Ríos, G.; Moats, M.S. Impurity Behavior in Cast Copper Anodes: Implications for Electrorefining in a Circular Economy. *Metals* **2025**, *15*, 113. [CrossRef]
33. Mossino, P. Some aspects in self–propagating high–temperature synthesis. *Ceram. Int.* **2004**, *30*, 311–332. [CrossRef]
34. Ely, F.G.; Barnhart, D.H. Coal Ash–Its effect on boiler availability. In *Chemistry of Coal Utilization Supplementary Volume*; John Wiley & Sons: New York, NY, USA, 1963; pp. 820–837.
35. Anderson, J.R. Solubility of Carbon in Molten Copper–Manganese and Copper–Nickel Alloys. Master's Thesis, Massachusetts Institute of Technology, Cambridge, MA, USA, 1946; p. 14.
36. Coetsee, T.; De Bruin, F. Chemical Behaviour of Copper in the Application of Unconstrained Cr–Ni–Al–Cu Metal Powders in Submerged Arc Welding: Gas Phase Thermodynamics and 3D Slag SEM Evidence. *Processes* **2023**, *11*, 351. [CrossRef]
37. Block–Bolten, A.; Eagar, T.W. Metal vaporization from weld pools. *Met. Mater. Trans. B* **1984**, *15*, 461–469. [CrossRef]
38. Merzhanov, A.G. Problems of combustion in chemical technology and in metallurgy. *Russ. Chem. Rev.* **1976**, *45*, 409–420. [CrossRef]

39. Song, J.; Guo, T.; Dine, W.; Yang, L.; Zhang, X.; Yu, Z.; Wu, J.; Zhang, J.; Fang, X. The effect of Al particle size on the thermal behvior and kinetics of Al– MnO_2 thermite system. *Adv. Mater. Sci. Eng.* **2020**, *2020*, 3097404. [CrossRef]
40. Olsφ, V.; Tangstad, M.; Olsen, S.E. Reduction kinetics of MnO–saturated slags. In Proceedings of the INFACON 8, The Chinese Society of Metals, Beijing, China, 7–10 June 1998; pp. 279–283.
41. Yang, J.; Kuwabara, M.; Sawada, T.; Sano, M. Kinetics of isothermal reduction of MgO with Al. *ISIJ Int.* **2006**, *46*, 1130–1136. [CrossRef]
42. Rafiei, M.; Ahmadnezhad, M.; Mostaan, H.; Saeidi, A. Reaction mechanism in SiO_2–MnO_2–Fe–Al system for producing ferrosiliconmanganese powder. *Adv. Powder Technol.* **2020**, *31*, 2613–2617. [CrossRef]
43. Ammasi, A. Effect of heating rate on decomposition temperature of Goethite ore. *Trans. Indian Inst. Met.* **2020**, *73*, 93–98. [CrossRef]
44. Liu, B.; Thomas, P.S.; Ray, A.S.; Williams, R.P. The effect of sampling conditions on the thermal decomposition of electrolyric manganese dioxide. *J. Therm. Anal. Calorim.* **2004**, *76*, 115–122. [CrossRef]